nature communications

Article

https://doi.org/10.1038/s41467-024-55603-1

Radiocarbon monoxide indicates increasing atmospheric oxidizing capacity

Received: 20 July 2024

Accepted: 18 December 2024

Published online: 02 January 2025

Check for updates

Olaf Morgenstern[1,2,7] ✉, Rowena Moss[1], Martin Manning[3], Guang Zeng[1,7], Hinrich Schaefer[1,8], Ilya Usoskin[4], Jocelyn Turnbull[5,6], Gordon Brailsford[1], Sylvia Nichol[1] & Tony Bromley[1]

Hydroxyl (OH) is the atmosphere's main oxidant removing most pollutants including methane. Its short lifetime prevents large-scale direct observational quantification. Abundances inferred using anthropogenic trace gas measurements and models yield conflicting trend estimates. By contrast, radiocarbon monoxide (^{14}CO), produced naturally by cosmic rays and almost exclusively removed by OH, is a tracer with a well-understood source. Here we show that Southern-Hemisphere ^{14}CO measurements indicate increasing OH. New Zealand ^{14}CO data exhibit an annual-mean decrease of 12 ± 2% since 1997, whereas Antarctic measurements show a December-January decrease of 43 ± 24%. Both imply similar OH increases, corroborating our own and other model results suggesting that OH has been globally increasing during recent decades. Model sensitivity simulations illustrate the roles of methane, nitrogen oxides, stratospheric ozone depletion, and global warming driving these trends. They have substantial implications for the budgets of pollutants removed by OH, and especially imply larger than documented methane emission increases.

The OH radical representing most of the atmosphere's oxidizing capacity is central to atmospheric chemistry due to its reactivity with almost all gaseous pollutants, both industrial and natural[1–3]. In particular, the important greenhouse gas methane is almost wholly removed by reaction with OH. Both its OH sink and consequently its emissions remain poorly constrained[4], making OH a key frontier in climate science. Efforts to mitigate methane would benefit from a better understanding of OH.

OH is very short-lived, highly variable, and challenging to measure[5,6], and due to insufficient coverage the few existing direct measurements of OH can neither sufficiently quantify its global abundance nor any possible trends[5,6] caused by anthropogenic air pollution and climate change. Concentrations of OH have been inferred using industrial trace-gas proxies removed by OH[7,8], with methyl chloroform (CH_3CCl_3, MCF) being the most commonly used[9,10]. However, emissions of MCF are now very substantially reduced due to the successful implementation of the Montreal Protocol, leading to large relative uncertainties in its budget[8]. Therefore, atmospheric inversions of OH, based on MCF, are under-constrained[11,12], and the trend estimates of OH based on such approaches can disagree with each other[11,13–15]. Emissions of industrial proxies are generally subject to large uncertainties, affecting their suitabilities as OH constraints[8,11–14,16]. Global chemistry models simulate OH[17,18], but a multitude of competing influences on OH and the lack of observational constraints cause model disagreements in OH abundances and the associated methane lifetime[12,16,19–21]. Recent modelling studies[18,22] suggest there was no

[1]National Institute of Water and Atmospheric Research (NIWA), 301 Evans Bay Parade, Wellington 6021, New Zealand. [2]School of Physical and Chemical Sciences, University of Canterbury, Private Bag 4800, Christchurch 8140, New Zealand. [3]School of Geography, Victoria University of Wellington, Kelburn Parade, Wellington 6012, New Zealand. [4]Sodankylä Geophysical Observatory, Space Physics and Astronomy Research Unit, University of Oulu, Oulu 90014, Finland. [5]Rafter Radiocarbon Laboratory, GNS Science, 30 Gracefield Road, Lower Hutt 5010, New Zealand. [6]CIRES, University of Colorado, Boulder, CO, USA. [7]Present address: Deutscher Wetterdienst, Frankfurter Str. 135, 63067 Offenbach am Main, Germany. [8]Present address: Royal Society Te Apārangi, 11 Turnbull St, Wellington 6011, New Zealand. ✉e-mail: olaf.morgenstern@gmail.com

https://doi.org/10.1038/s41467-024-55603-1

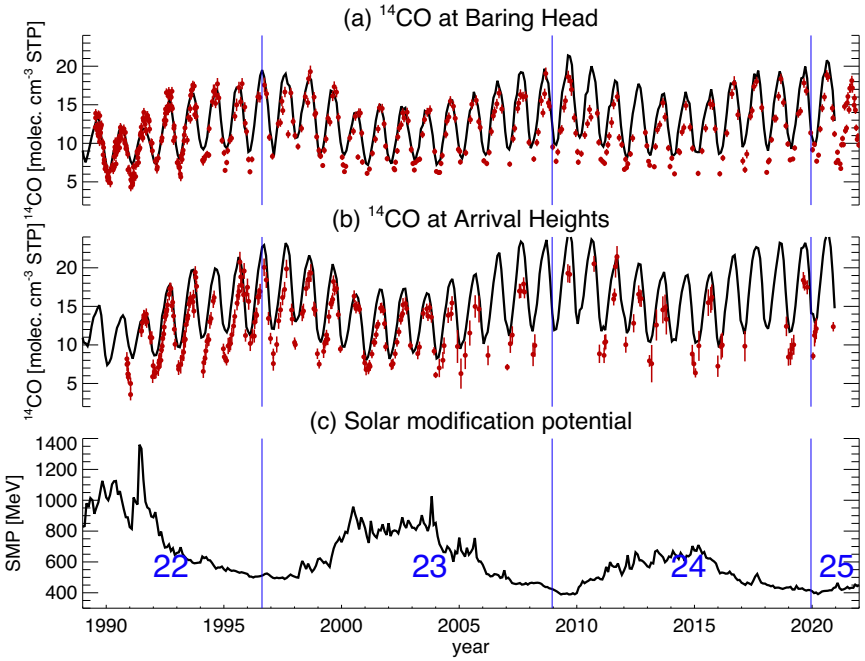

Fig. 1 | The Southern-Hemisphere ^{14}CO measurements and model results and the solar modulation parameter as functions of time. (red) ^{14}CO measurements at (**a**) Baring Head and (**b**) Arrival Heights. The red vertical bars reflect the standard measurement errors. (black solid lines) Monthly-mean surface ^{14}CO, interpolated to the locations of Baring Head and Arrival Heights, as simulated by the NIWA-UKCA model (see below and section " Galactic ^{14}C production and the NIWA-UKCA model"). **c** Monthly-mean "solar modulation parameter" (SMP, in MeV) since 1989 (https://cosmicrays.oulu.fi/phi/Phi_Table_2017.txt). The blue digits and vertical bars conventionally enumerate and bound, respectively, the solar cycles (https://www.spaceweather.com/en/solar-activity/solar-cycle/historical-solar-cycles.html).

substantial change in OH throughout the industrial period, but then an increase occurred since the 1980s (which may have been associated with a decrease in CO emissions in recent decades[23]), whereas OH trends inferred using industrial tracers show no change or a decrease after the mid-2000s[10,24].

Here we analyze the longest and most consistent radiocarbon monoxide (^{14}CO) records from two remote Southern-Hemisphere locations, Baring Head (New Zealand) and Arrival Heights (Antarctica), for evidence of trends in the atmospheric oxidizing capacity[25–27], Supplementary Table 1. ^{14}CO complements industrial proxies as a constraint on OH because it is almost exclusively removed by OH with a well-defined natural source[15,25,26,28,29]. Most ^{14}CO forms in the nuclear cascade initiated by energetic cosmic-ray particles throughout the stratosphere and troposphere. This cosmogenic ^{14}CO production peaks in the lower stratosphere over both magnetic poles where the geomagnetic shielding of cosmic rays is minimal[15,30–32]. The production of ^{14}CO is much better quantified than emissions of MCF [section "Galactic ^{14}C production and the NIWA-UKCA model",[15]]. However, the relatively short global lifetime and inhomogeneous distribution of ^{14}CO mean that ^{14}CO is mainly a constraint on regional OH, whereas MCF imposes a global constraint, with the greatest sensitivity to variations in tropical OH[27]. Earlier studies have used ^{14}CO to constrain the OH abundance[25–27]. However, the lack of long-term ^{14}CO time series has previously precluded its usage as a constraint on multi-decadal OH trends[26].

Results

Normalization of the ^{14}CO data

Two dominant natural influences on these measurements become evident (Fig. 1a,b) once corrected for instrumental artefacts and post-collection production of ^{14}C in the sampling flasks (section "^{14}CO records"): The first is seasonality, with minima during February-March and maxima during August-September. The seasonal cycle is due to OH-induced loss of ^{14}CO and seasonally varying stratosphere-to-troposphere transport. OH production requires sunlight; hence the ^{14}CO loss rate is seasonal, particularly at Arrival Heights, which is in darkness for 5 months of the year. Secondly, with the time series now covering three 11-year solar cycles, the influence of the solar state is obvious. Solar activity influences the interplanetary magnetic field, which modulates the flux of energetic cosmic rays impinging on the atmosphere near both magnetic poles to produce ^{14}C, which rapidly oxidizes to ^{14}CO (section " Galactic ^{14}C production and the NIWA-UKCA model"). This modulation is often quantified via the solar modulation parameter [SMP[32–34], Fig. 1c]. The SMP and ^{14}CO anticorrelate at both stations (Fig. 1), and the SMP exhibits a long-term declining trend since 1989 superimposed on the 11-year solar cycle (Fig. 1c).

To reveal long-term trends in ^{14}CO we normalize the measurements. We denote by

$$^{14}\mathrm{CO}_{\mathrm{norm}} = \frac{^{14}\mathrm{CO}}{\langle ^{14}\mathrm{CO}\rangle} \quad (1)$$

the ^{14}CO data normalized for seasonal and solar influences. $\langle ^{14}\mathrm{CO}\rangle$ is a regression fit to the ^{14}CO measurements (section "Normalization for seasonal and solar influences"). Pertinent long-term trends are apparent in $^{14}\mathrm{CO}_{\mathrm{norm}}$ (Fig. 2). At both locations, the data indicate a peak of $^{14}\mathrm{CO}_{\mathrm{norm}}$ around 1997 followed by a period of decline. The large negative anomalies in $^{14}\mathrm{CO}_{\mathrm{norm}}$ around 1991/1992 and positive anomalies around 1997/1998 are consistent with variations in OH[26] that have been attributed to the eruption of Mt Pinatubo in 1991, which strengthened OH[35], and the 1997 Indonesian wildfires which produced large amounts of pollutants that suppressed global OH[36,37].

At Baring Head, the post-1997 trend of $-0.50 \pm 0.09\%\ \mathrm{a}^{-1}$, corresponding to a ~ 12 ± 2% decrease in $^{14}\mathrm{CO}_{\mathrm{norm}}$ over the period 1997-2022, is significant throughout most of the year. (The error calculation used here is detailed in section "Uncertainty calculation". All uncertainties are at 68% confidence.) However there is noteworthy

https://doi.org/10.1038/s41467-024-55603-1

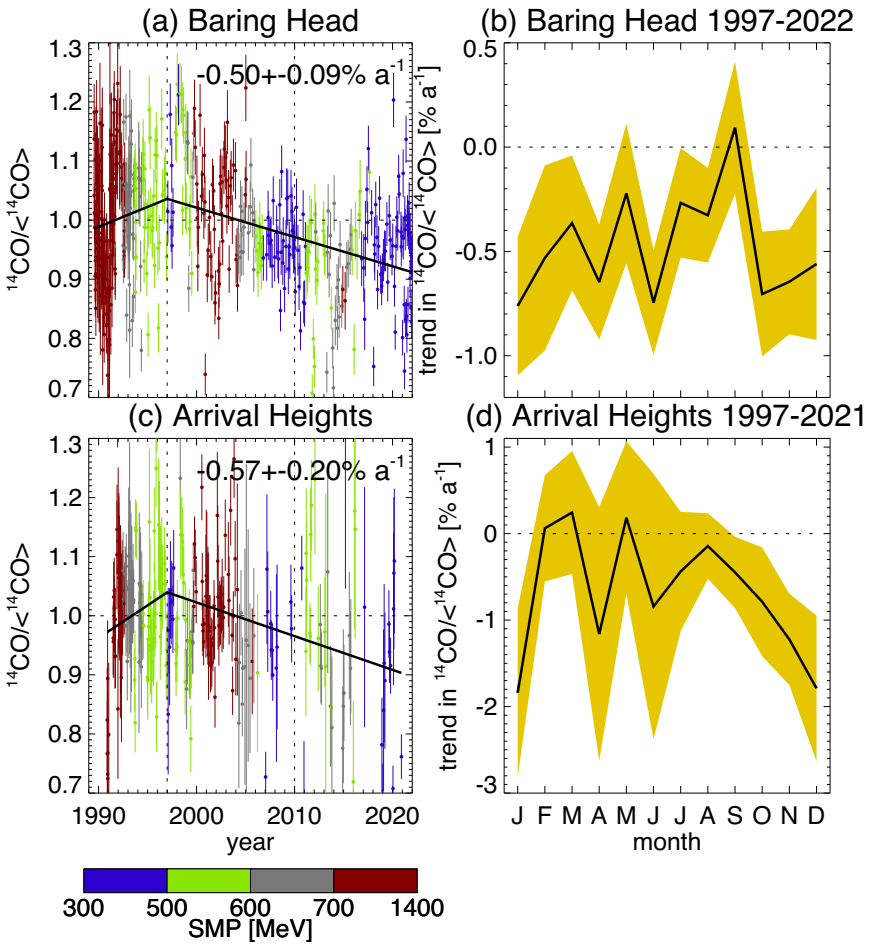

Fig. 2 | Normalized ^{14}CO measurements and their trends. a, c Normalized measurements $^{14}CO_{norm}$ as functions of the times of the measurements (section "Normalization for seasonal and solar influences"). The thick black lines mark least-squares piecewise linear regression fits for central nodes in 1997. Colours mark the solar modulation parameter (SMP) at the times of the measurements. Vertical lines denote the standard measurement errors. The numbers are the post-1997 trends and their uncertainties. **b, d** Post-1997 trends in $^{14}CO_{norm}$ (% a^{-1}) and their standard errors as functions of the month of the year, using the same piecewise-linear fitting method as used in panels (**a**) and (**c**) applied to subsets of the data grouped by month.

multi-year variability in this period of decline, such as anomalously low values of $^{14}CO_{norm}$ around 2015 and a partial recovery thereafter.

At Arrival Heights, we find a substantial ~1.8 ± 1% a^{-1} decrease during December and January, or ~ 43 ± 24% over 1997-2021, but the negative trend is significant only from October to January (Fig. 2). This is consistent with the strong seasonality of ^{14}CO removal by OH, which at polar latitudes only exists during spring and summer, and therefore here OH only drives ^{14}CO trends during the polar day.

Potential causes for ^{14}CO trends not involving OH

Multidecadal influences on ^{14}CO include the recovery from the spike of atmospheric ^{14}C caused by atmospheric nuclear bomb explosions, which ceased in 1963, and the Suess effect of dilution of ^{14}C in the climate system by the combustion of ^{14}C-depleted fossil fuels. Both factors are reflected in the Baring Head $\Delta^{14}CO_2$ signal, which between 1997 and 2022 decreased from 110‰ to 3‰ [i.e. a ~10% reduction in $^{14}C/C$[38], extended data available at https://gaw.kishou.go.jp]. Similar trends are occurring around the globe[39]. Assuming this decrease is instantly reflected in biological material (via photosynthetic uptake) and in biomass-burning CO, which contributes ~2 molecules cm^{-3} to ^{14}CO at both locations[15,40], its impact of 0.06 molecules cm^{-3} $decade^{-1}$ or 0.2 molecules cm^{-3} over 1989–2022 is an order of magnitude smaller than the actual ^{14}CO trend at Baring Head. Other ^{14}CO sources, such as the oxidation of $^{14}CH_4$, also do not explain the ^{14}CO trends[15]. During much of the post-1989 period of interest here, $^{14}CH_4$ has been on an increasing trend[41,42], ruling out $^{14}CH_4$ as a contributing factor in the decrease found here of $^{14}CO_{norm}$.

The seasonality of the $^{14}CO_{norm}$ trends at Arrival Heights suggests that changes in transport from the lower stratosphere (where ^{14}CO production and abundance maximize, section "Galactic ^{14}C production and the NIWA-UKCA model") are not the leading cause of these trends. Downward stratosphere-to-troposphere transport maximizes in austral winter and spring[43], but large negative trends in $^{14}CO_{norm}$ occur in December and January. This detail rules out transport from the stratosphere as the leading cause of the ^{14}CO trends at Arrival Heights.

Modelled ^{14}CO and OH

To link the ^{14}CO observations to OH, we use the NIWA-UKCA atmosphere-only chemistry-climate model, expanded to include a representation of only cosmogenic ^{14}CO production and loss to OH. Unlike some previous approaches[44], NIWA-UKCA simulates OH interactively as part of a predictive stratosphere-troposphere chemistry scheme. More details are in section "Galactic ^{14}C production and the NIWA-UKCA model". NIWA-UKCA is free-running, i.e. simulated weather-related variations of ^{14}CO are not expected to correlate with observed variations.

The model closely reproduces key characteristics of the data, including the seasonal cycle, the solar dependence, and larger ^{14}CO

https://doi.org/10.1038/s41467-024-55603-1

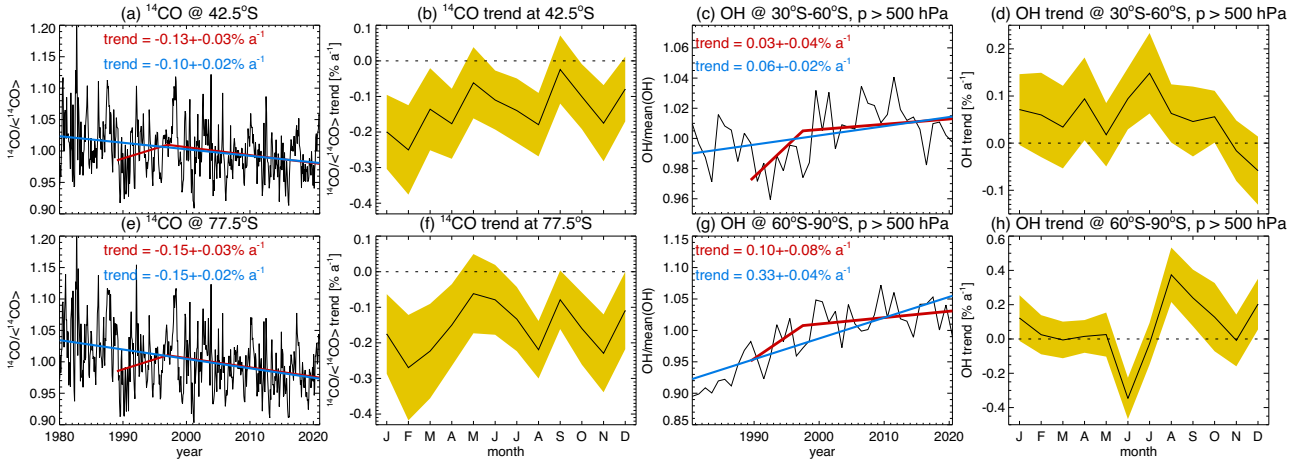

Fig. 3 | Normalized ^{14}CO model results and their trends. a, e Zonal- and monthly-mean surface $^{14}CO_{norm}$ derived from the NIWA-UKCA simulation at the latitudes 42.5°S and 77.5°S (the model latitudes closest to Baring Head and Arrival Heights). Red: Piecewise linear fits with nodes in 1989, 1997, and 2021. Blue: Simple linear fit for the whole simulation period (1980-2020). The trend values are for (red) 1997–2020, and (blue) 1980–2020. **b, f** 1997–2020 trends in ^{14}CO resolved by month, with their uncertainty ranges at 68% confidence. **c,g** Annual-mean OH (relative to its mean for 1989–2009) averaged by concentration over the region below 500 hPa. **c** Mid-latitude average (30°S-60°S). **g** Polar average (60°S-90°S). Red and blue lines are the trends as for (**a**) and (**e**). **d, h** Monthly trends for 1997-2020 in normalized OH, in % a^{-1}, with the 68% confidence uncertainty ranges. Note the different scales.

values at Arrival Heights than at Baring Head (Fig. 1). Replacing in Fig. 1 monthly mean with 10-daily instantaneous ^{14}CO makes no major difference.

The model simulates variability in $^{14}CO_{norm}$ (Fig. 2 and section "Normalization for seasonal and solar influences") similar to what is seen in the observations, regarding both the annual- and shorter-scale variability as well as multi-year variations such as those highlighted by the piecewise-linear fits (red lines in Fig. 3). In particular, the model simulates a trough of $^{14}CO_{norm}$ around 1990, a peak around 1998, and another minimum around 2015. We note the good similarity of these variations with the observations, although the model generally simulates smaller amplitudes than those found in the observations. Superimposed on these variations, however, are long-term negative trends of simulated $^{14}CO_{norm}$ at both locations (−0.10% a^{-1} at Baring Head and −0.15% a^{-1} at Arrival Heights for the period 1980-2020, amounting to decreases of $^{14}CO_{norm}$ by 4.1 and 6.1% respectively). It therefore appears that the decreases in observed $^{14}CO_{norm}$ highlighted for 1997-2020 in Fig. 2 are best understood as episodes of longer-term $^{14}CO_{norm}$ decreases that have been occurring over several decades[18]. At both locations these trends are substantially smaller than in the observations. This is discussed in section "Discussion".

Next we assess simulated OH. Firstly, at both locations the pertinent long-term declines in $^{14}CO_{norm}$ have coincided with concurrent multidecadal increases in OH. In fact this OH increase, in our model, is nearly global (Fig. 4), as has been found in some previous CMIP6 modelling studies e.g.[16,18]. (As a caveat, only three CMIP6 models are suitable for this analysis, one of which (UKESM1) has some heritage and largely the chemistry scheme in common with NIWA-UKCA.) Resultant annual trends for mid-latitude OH integrated below 500 hPa (Fig. 3c) are of comparable relative magnitude but opposite in sign to those for surface $^{14}CO_{norm}$, for both 1980-2020 and 1997-2020, but these trends are altitude-dependent (see below). As for $^{14}CO_{norm}$, the OH trends occur almost year round (Fig. 3d), and relative seasonal trends for OH are mostly similar to those of $^{14}CO_{norm}$. This similarity strongly suggests that indeed the OH trends cause the $^{14}CO_{norm}$ trends.

At 77.5°S, OH is dominated by photochemistry during peak summer (December / January). In these months significant positive trends in OH occur (Fig. 3h), which are similar in magnitude to the $^{14}CO_{norm}$ trends at 77.5°S but opposite in sign (Fig. 3f). The large relative trends in OH simulated for the winter months have no bearing on ^{14}CO as they occur against near-zero abundances of OH.

To put these findings into perspective, our assessment, based on NIWA-UKCA (Fig. 4) and[18], is that trends of $^{14}CO_{norm}$ derived from our measurements may be representative of downward trends in $^{14}CO_{norm}$ and upward trends in OH that have occurred throughout most of the Southern Hemisphere. OH trends here largely mirror $^{14}CO_{norm}$ trends, but are of opposite sign. At southern high latitudes, larger absolute trends occur for OH than for $^{14}CO_{norm}$ (Fig. 3e,g). Also noteworthy are the substantially larger absolute trends in OH and $^{14}CO_{norm}$ occurring in the Northern Hemisphere. Positive OH trends have been associated with increasing emissions of NO_x that are concentrated in the Northern Hemisphere[18]. A factor decomposition of the OH trend (Fig. 7) indicates that at Baring Head growing NO_x emissions and increasingly also global warming are driving positive OH trends, whereas at Arrival Heights the leading factor is Antarctic ozone depletion. At both locations, methane increases drive decreases in OH[18]. Gaubert et al.[23] find that CO emission decreases in Europe and North America since the 1980s drive OH increases. At the two Southern-Hemisphere locations, such CO decreases do not play a leading role in causing the simulated OH increase but are more important in the Northern Hemisphere (not shown).

An observation-based analysis equivalent to the one performed here for Southern-Hemisphere OH is unfortunately presently not possible for the Northern Hemisphere due to the unavailability of sufficiently long and consistent ^{14}CO measurements from there. Hence while there is model agreement that substantial OH increases have happened there, and NIWA-UKCA simulates substantial Northern-Hemisphere negative trends also for $^{14}CO_{norm}$, these findings do remain mere model indications in need of observational validation.

The NIWA-UKCA simulated zonal-mean OH trend patterns are similar to the OH change patterns since 1850 found for three CMIP6 models. Given that trends prior to 1980 were small and these changes have occurred predominantly since 1980, we find that the NIWA-UKCA OH trends are quantitatively similar and consistent with those simulated by the CMIP6 models[18].

Discussion

The observed multidecadal decreases in $^{14}CO_{norm}$ are the first strong evidence for positive multi-decadal OH trends at southern mid- and high

https://doi.org/10.1038/s41467-024-55603-1

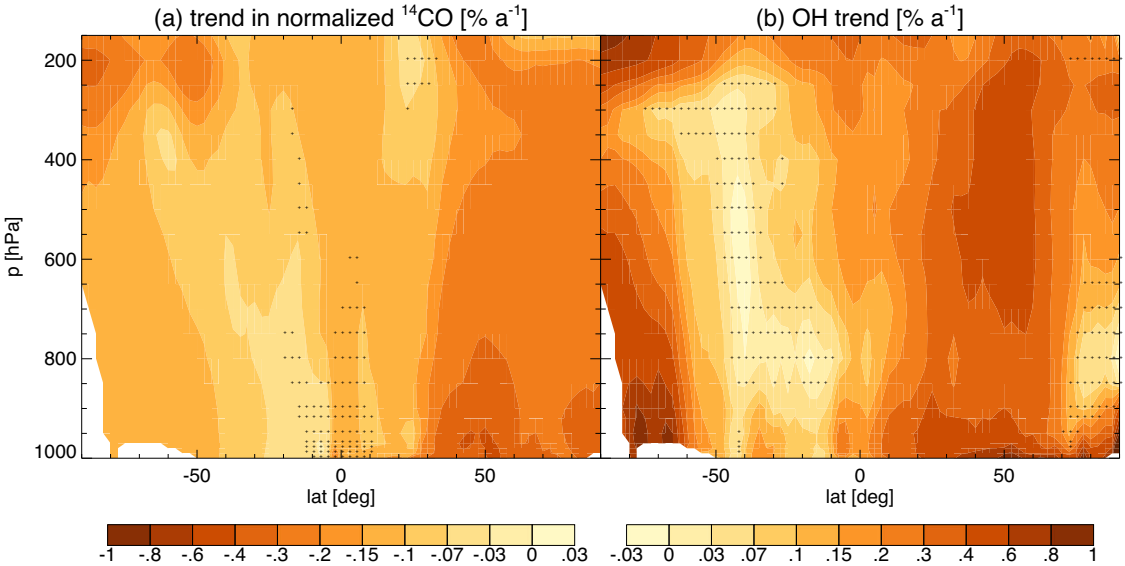

Fig. 4 | Global $^{14}CO_{norm}$ and OH trends. a Trend (% a^{-1}) in simulated annual- and zonal-mean $^{14}CO_{norm}$, relative to its 1989–2010 mean, for the period 1980–2020. Stippling means the trends are insignificant at 68% confidence. **b** Same but for the annual- and zonal-mean OH concentration, relative to its 1989–2010 mean.

latitudes. In chemistry-climate model simulations, global multi-decadal OH increases are mainly caused by increasing ozone precursor emissions (especially NO_x), with an offset by increasing methane which suppresses OH[12,18,37], and references therein. This explains the much larger OH and $^{14}CO_{norm}$ trends simulated for the more industrialized Northern Hemisphere, compared to the South (Fig. 4). Industrial ozone precursor emissions are relatively small at southern mid-latitudes, yet even for this remote region the ^{14}CO measurements imply positive trends in OH.

In addition to short-lived pollutants, increases in ozone-depleting substances (ODSs) until the late 1990s have caused an increase in modelled OH at southern high latitudes, due to the effect of changes in the overhead ozone column that impact the OH production through ozone photolysis[18]. This effect explains a part of the large relative trend in OH over Antarctica evident in our model simulations (Fig. 4). However there is no evidence of a change in the trend of OH after 2000 (when ODSs stabilized, Fig. 3g), so this cannot be the only explanation.

Whilst our model NIWA-UKCA qualitatively corroborates this increase in OH, it simulates only about 1/4 of the observed $^{14}CO_{norm}$ trends calculated for the two stations. Since NIWA-UKCA OH trends are similar to those simulated by three CMIP6 models, we suggest that this model behaviour might reflect a misrepresentation of Southern-Hemisphere OH trends also by the three CMIP6 models considered by[18].

As noted, at least at Baring Head, the discrepancy between the simulated and observed ^{14}CO trend might indicate that NIWA-UKCA does not correctly represent the cancellation of opposing effects there. In particular, it is possible that NIWA-UKCA does not well represent the low NO_x abundance in the remote Southern extratropics. NO_x in this region is the product of relatively poorly understood processes including long-range transport of odd nitrogen compounds from industrialized regions and lightning. In the more polluted Northern Hemisphere, these processes are relatively less important, meaning that the deficiencies found here for the Southern extratropics may not apply to the Northern Hemisphere. Irrespectively of the precise causes, the near-complete cancellation of the two competing influences of NO_x and methane makes the net OH trend at southern midlatitudes highly sensitive to shortcomings in the representation particularly of NO_x (section " Galactic ^{14}C production and the NIWA-UKCA model").

Plausibly then the observational $^{14}CO_{norm}$ trends since 1997 discerned here, supported by modelling studies[16,18,37], and references therein, suggest multi-decadal global-scale increases of OH that may have started in around 1980[18]. Given various limitations affecting all existing studies of this topic, including our own, we do, however, consider that further research, using both observations and models, would help corroborate this statement. For example, this inference is notwithstanding conclusions based on recent MCF inversions and similar techniques that have found no significant change or a decrease in the global OH burden after the mid-2000s. Naus et al.[24] only focus on variations not trends as they adjust inferred MCF emissions to match the observed MCF variations. A study that derives OH from the inversion of multiple industrial proxies[45] finds stabilization of OH over a shorter period (2004-2020). This is likely consistent, within statistical uncertainties, with our model results and the ^{14}CO observations, given the multiannual variations of $^{14}CO_{norm}$ after 2004 alluded to above (Fig. 2a).

A pertinent decades-long strengthening trend in the oxidizing capacity implies a corresponding additional increase in methane emissions required to balance its increasing sink, e.g. 23 Gt a^{-1} for 1986-2010[37], relative to a scenario with stable OH such as [46]. Such an increase compares to other sizeable sources of methane, e.g. global emissions from rice paddies [30 Gt a^{-1}, out of a total CH_4 emission strength of ~ 576-727 Tg a^{-1} in 2008-2017[46]].

Maintaining the observations since 1989 has enabled the detection reported here of a multidecadal strengthening of the atmospheric oxidizing capacity in the Southern extratropics. It exemplifies the value of environmental monitoring. In some situations these measurements have to be sustained for decades before a trend analysis can yield valuable insights into environmental change. More ^{14}CO data from the more polluted Northern Hemisphere, where according to modelling studies larger OH trends occur, would be valuable to better constrain global OH trends. In due course a nascent ^{14}CO measurement network, complementing the two stations considered here, may provide this much needed global coverage[47].

Methods

^{14}CO records

Air samples are taken only when air arriving at the stations is free of locally produced contamination and representative of clean marine or

https://doi.org/10.1038/s41467-024-55603-1

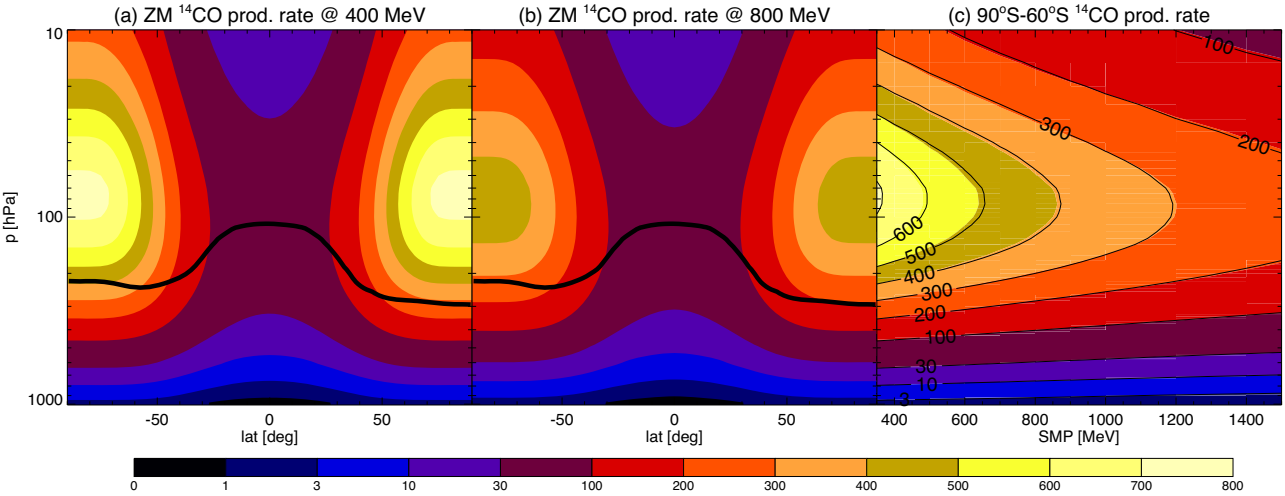

Fig. 5 | The ^{14}CO galactic source function. a, b Zonal-mean (ZM) rate of production of ^{14}CO (molecules cm^{-3} year^{-1} STP) at SMPs of 400 and 800 MeV. Thick contour: For illustration, the approximate annual-average tropopause pressure. **c** ^{14}CO production rate averaged over the Antarctic polar cap (90°S-60°S) as a function of the SMP (section "Normalization of the ^{14}CO data") and pressure. Contours: Polynomial regression fit to the logarithm of the ^{14}C production rate (equation 2).

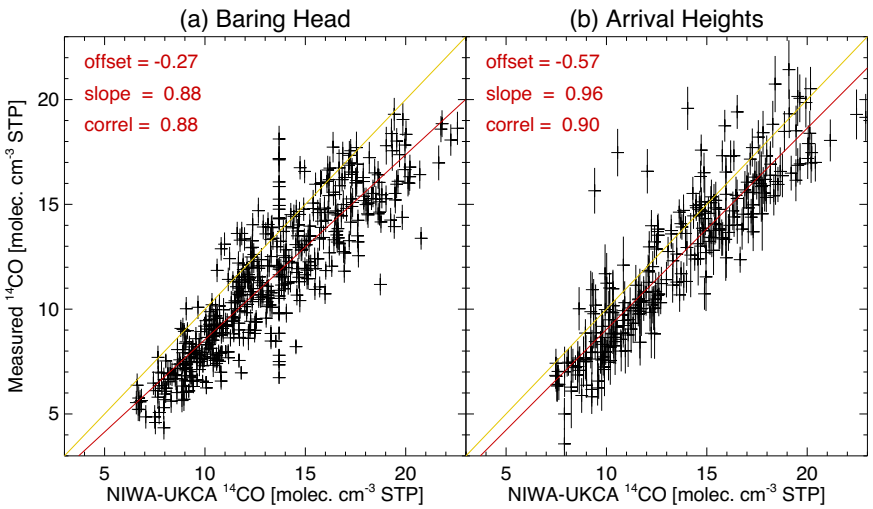

Fig. 6 | Comparison of observed and modelled ^{14}CO. Symbols: ^{14}CO measurements versus corrected NIWA-UKCA ^{14}CO. Vertical bars indicate the standard measurement errors. Yellow lines: diagonals. Red lines: Least-squares linear fits. Red labels: Linear fit and Pearson's correlation coefficients. **a** Baring Head. **b** Arrival Heights.

polar conditions. The ^{14}CO content is determined using accelerator mass spectrometry, preceded by complex sample preparation including removal of CO_2, conversion of CO to CO_2, dilution with ^{14}C-free CO_2 gas, as well as stable isotopic measurement[26,48]. Measured ^{14}CO values are corrected to account for production of ^{14}CO within the flasks during storage and transport. Longer storage times and larger cosmic-ray fluxes lead to larger corrections and associated uncertainties at Arrival Heights than at Baring Head. More details on the measurement process, post-measurement corrections, and measures taken to ensure the absence of analytical artefacts are in the Supplementary Sections 1 to 5.

Galactic ^{14}C production and the NIWA-UKCA model

While the flux of galactic cosmic rays (GCR) is considered nearly constant in the local galactic environment, it changes significantly in the vicinity of the Earth as a result of the modulation by the solar wind and the embedded heliospheric magnetic field. The modulation process is complex [e.g. [49]] but for practical purposes it is often parameterized via a single synthetic solar modulation parameter (SMP) which roughly corresponds to the average rigidity loss of cosmic-ray particles inside the heliosphere in the framework of the force-field approximation[33,50]. Values of the SMP are typically assessed using data from the global network of ground-based neutron monitors[33,51]. Here we use the SMP, obtained following the methodology by[51], available at https://cosmicrays.oulu.fi/phi/phi.html, as a continuously updated SMP dataset. The reconstructed SMP values may slightly depend on the assumed shape of the unmodulated GCR spectrum. However, since different reconstructions are linearly scalable to each other[51,52], the analysis presented here is insensitive to the exact choice of the SMP dataset because the regression fit $\langle^{14}CO\rangle$ (equation 1) is invariant under a linear transformation of the SMP (equations 4, 5).

Cosmogenic ^{14}CO production can thus be thought of as a function of magnetic latitude, pressure, and the SMP, where the "magnetic latitude" is the latitude relative to the magnetic, not the geographic, poles. In conventional, geographic latitude-longitude coordinates, this implies an explicit dependence also on longitude. The generation function[32] is displayed in Fig. 5.

The production maximizes over both poles and is decreasing markedly for an increasing SMP. The contours in Fig. 5c represent

https://doi.org/10.1038/s41467-024-55603-1

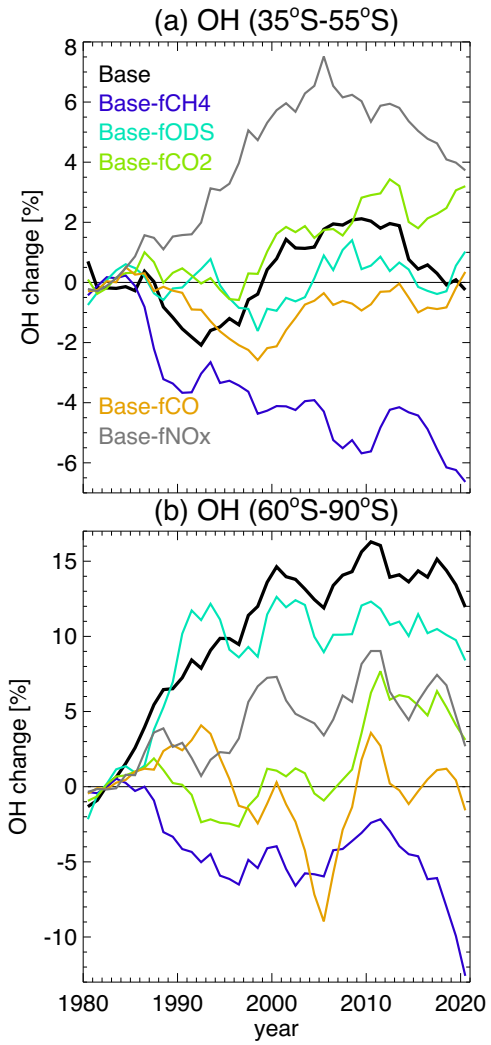

Fig. 7 | Modelled sensitivity of OH to anthropogenic pollution. Displayed are changes in annual-mean OH, vertically integrated between the surface and 500 hPa, averaged over middle and high southern latitudes as indicated. All curves are smoothed with a 5-year symmetric boxcar filter and expressed relative to their 1980–1984 means. Black: base, all-forcings simulation. Colours: Differences in integrated OH between the base and the sensitivity simulations, each with one forcing held constant, relative to the base simulation, in percent. **a** Southern mid-latitude average (35°S-55°S). **b** Southern polar-cap average (60°S-90°S).

Table 1 | The regression coefficients defining ⟨^{14}CO⟩

	i	*j* = 0	1	2
BHD				
P_{ij}	0	11.611	−2.394	−0.478
	1	−1.387	0.294	−0.073
	2	0.071	−0.130	0.071
Q_{ij}	0		−3.430	−0.211
	1		0.337	0.147
	2		0.000	−0.058
R_{ij}	1	0.044	0.235	
U_{ij}	1		0.115	
ARH				
P_{ij}	0	12.472	−2.717	−0.826
	1	−2.093	−0.371	−0.278
	2	0.449	0.195	0.124
Q_{ij}	0		−3.948	−0.417
	1		0.192	0.335
	2		0.367	0.077
R_{ij}	1	0.455	−0.188	
U_{ij}	1		0.135	

The coefficients P_{ij}, Q_{ij}, R_{ij}, and U_{ij} (all in molecules cm^{-3}) appear in equations (4) and (5) for Baring Head and Arrival Heights.

least-squares fits of the form

$$E(p,s) = \exp\left[\sum_{i=0}^{2} U_i(p)s^i\right], \quad (2)$$

expressing the logarithm of the production function E as a quadratic polynomial in the SMP s with coefficients U_i depending on pressure p. Figure 5 illustrates that ^{14}CO is dominantly produced over both poles, with production rates around two orders of magnitude larger at 100 hPa than at the surface. However, transport times between the lower stratosphere and the surface can be considerable, relative to the global mean lifetime of ^{14}CO, especially during summer when upward motion prevails over much of the polar stratosphere, inhibiting any ^{14}CO reaching the surface. These factors help explain the large seasonality in ^{14}CO evident in Fig. 1.

We have implemented a ^{14}CO tracer including its cosmogenic source in the established NIWA-UKCA chemistry-climate model. In brief, the model comprises an interactive chemistry scheme representing O_x-HO_x-NO_x-VOC-halogens chemistry suitable for the troposphere and stratosphere, targeting a realistic representation of ozone at global scales[53–56]. The model is low-resolution (3.75° × 2. 5° in longitude and latitude, with 60 levels extending to 84 km, ca. 25 of which are in the troposphere). Photolysis rates in the model respond interactively to variations in ozone, but scattering and absorption due to aerosol are ignored. Volcanic aerosol affects stratospheric chemistry via an externally supplied surface area density climatology. The set-up used here is identical to the model used for the Chemistry-Climate Model Initiative (CCMI) 2022 simulations[57] but the model chemistry scheme is expanded to simulate cosmogenic ^{14}CO production, its losses to OH and deposition to the Earth's surface, and transport. The loss rates to OH and to dry deposition are the same as for regular CO. In particular, the reaction rate coefficient r associated with OH + ^{14}CO is represented as[58],

$$r = \frac{1.44 \cdot 10^{-13}}{1 + \nu/4.2 \cdot 10^{19}}\,\mathrm{cm^3 molecule^{-1} s^{-1}}, \quad (3)$$

where ν is the molecular number density in molecules cm^{-3}. The model does not explicitly represent any other sources of ^{14}CO such as biogenic recycling or $^{14}CH_4$ oxidation. This means also the nuclear bomb signal is not simulated.

Using NIWA-UKCA, we conduct a base simulation covering 1980-2020 (41 years), driving the model with 6th Coupled Model Intercomparison Project (CMIP6) "historical and Shared Socioeconomic Pathway (SSP) 245[59] forcings and Hadley Centre Ice and Sea Surface Temperature HadISST.2,[60] ocean surface forcings. In postprocessing we adjust the simulated cosmogenic ^{14}CO to account for a 94% quantum yield of ^{14}CO production from ^{14}C produced by cosmic rays[40,47,61]. Furthermore we account for biogenic recycling by adding $1.27 \cdot 10^{-12}$[CO], using the CO field simulated by the model[26]. ^{14}C/C = $1.27 \cdot 10^{-12}$ is equivalent to assuming a 1 molecule cm^{-3} contribution of biogenic recycling for 30 ppbv of ambient CO[15]. (This correction would be more questionable in the Northern Hemisphere where this rule may not apply, due to more substantial and variable contributions of ^{14}C-depleted fossil-fuel burning to ambient CO.) Both

https://doi.org/10.1038/s41467-024-55603-1

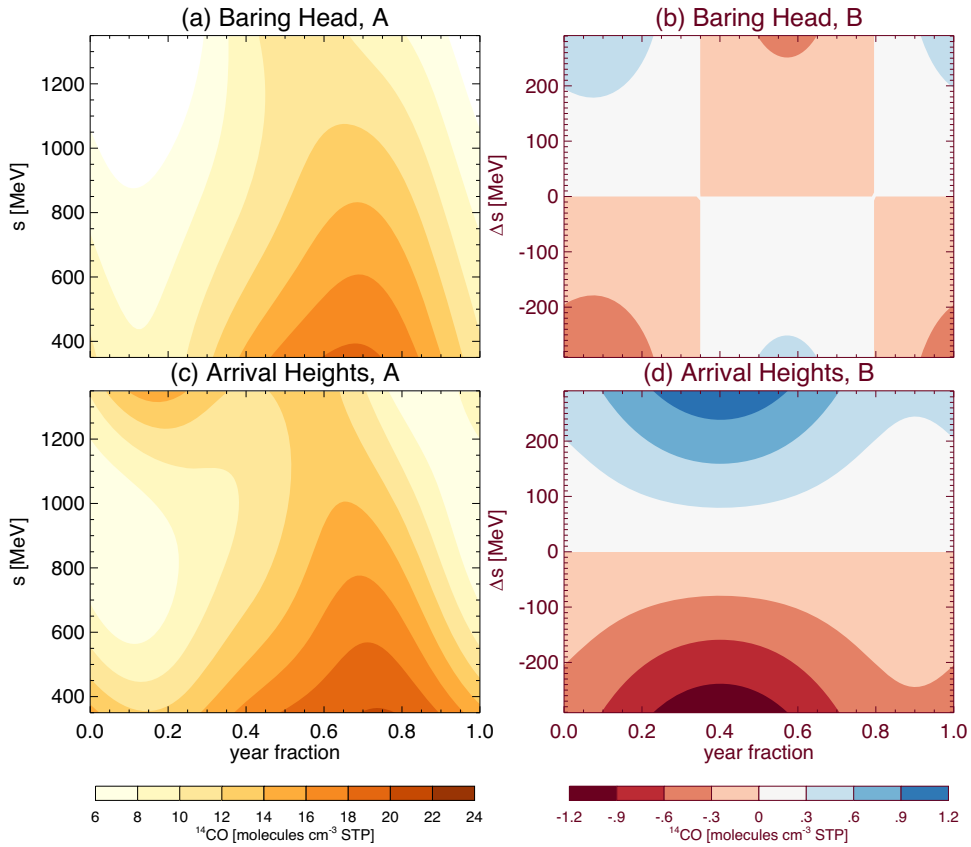

Fig. 8 | Graphical representations of regression fits ⟨^{14}CO⟩. a, c Component of regression fit $A(s, t)$, where s is the SMP (section "Normalization of the ^{14}CO data"). **b,d** Component of regression fit $B(\Delta s, t)$, where Δs is the trend in the smoothed SMP (section "Normalization of the ^{14}CO data"). **a, b** Baring Head. **c,d** Arrival Heights.

adjustments are practically immaterial after normalization of ^{14}CO (section "Normalization for seasonal and solar influences").

Figure 6 suggests that the model slightly overestimates ^{14}CO (more at Baring Head than at Arrival Heights) but produces high correlations with the observed ^{14}CO values.

We furthermore conduct all-minus-one sensitivity simulations in which one forcing agent is held constant at 1980 levels, but all other forcings develop in the same way as in the base simulation. For CO_2, apart from holding the atmospheric mixing ratio of CO_2 constant, in an effort to also suppress the warming caused by CO_2 this also involves prescribing SSTs and sea ice concentrations as annually periodic lower boundary conditions following their 1980 annual cycles.

Essentially, at mid-latitudes the leading influences on tropospheric OH are CH_4, increases of which drive a decrease in OH, and NO_x emissions, increases of which drive a similarly sized increase in OH (Fig. 7). Other drivers (ODSs, CO_2, CO) play smaller roles, although at the end of the simulation, the influence of CO_2 and global warming is as large as that of NO_x. At Arrival Heights, the leading influence is due to ODSs which drive an overall increase in OH, partially offset by CH_4 driving a decrease. Here we find less cancellation of opposing effects, explaining the much larger but seasonal trends in OH and ^{14}CO in the base simulation. Not shown are the influences of VOCs which are small at both locations. These trends are consistent with the OH trends simulated by the three CMIP6 models analyzed by[18].

Normalization for seasonal and solar influences

We use the following regression model to represent the 1989–2009 ^{14}CO measurements at Baring Head and Arrival Heights. The later ^{14}CO data are used in an out-of-sample test of the suitability of the regression model, see below:

$$A(s,t) = \sum_{i=0}^{2} s(t)^i \left\{ \sum_{j=0}^{2} P_{ij} \cos(2\pi j t) + \sum_{j=1}^{2} Q_{ij} \sin(2\pi j t) \right\} \quad (4)$$

$$B(\Delta s, t) = \Delta s(t) \{ R_{10} + R_{11} \cos(2\pi t) + U_{11} \sin(2\pi t) \} \quad (5)$$

$$\langle {}^{14}\mathrm{CO} \rangle (s, \Delta s, t) = A + B \quad (6)$$

Here t is time, measured in years, and s represents the SMP, non-dimensionalized by removing the mean of the monthly-mean SMP values (620 MeV) and then dividing by their standard deviation (182 MeV) for January 1989 to December 2021. $\Delta s(t) = \bar{s}(t) - \bar{s}(t - 1\,\mathrm{a})$, where the overbars indicate smoothing with a 13-months symmetric boxcar filter, and $\bar{s}(t - 1\,\mathrm{a})$ is $\bar{s}$ evaluated one year before t. Its presence accounts for a slight phase shift between s and ^{14}CO, indicating that measured ^{14}CO is influenced by solar activity occurring before the measurements are taken. The 18 coefficients P_{ij}, Q_{ij}, R_{ij}, and U_{ij} in equations (4) and (5) minimize the squared residual $\sum_k \epsilon_k^{-1} \left[{}^{14}\mathrm{CO}_k - \langle {}^{14}\mathrm{CO} \rangle (s_k, \Delta s_k, t_k) \right]^2$, where k enumerates the measurements at either location, and ϵ_k are the observational measurement uncertainties. The above ansatz amounts to a multilinear regression of the ^{14}CO measurements (in molecules cm^{-3} STP). Importantly it only allows for seasonal and solar influences on ^{14}CO, and excludes any other influences such as those associated with long-term variations in OH. For both locations, the solutions to the linear regression are listed in Table 1.

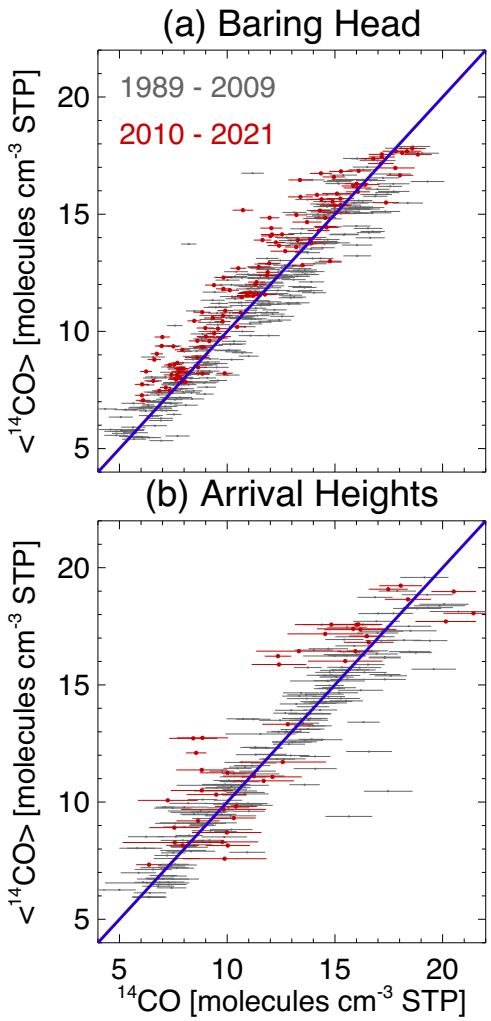

Fig. 9 | ^{14}CO measurements versus the regression fits $\langle^{14}CO\rangle$. Grey: Measurements taken before 2010. Red: Measurements after 2010. (**a**) Baring Head. (**b**) Arrival Heights. The horizontal lines mark the standard measurement errors. The blue lines mark the diagonals.

The regression fits decompose into sums of a term $A(s, t)$, associated with the regression coefficients P_{ij} and Q_{ij} (equation 4), and a further term $B(\Delta s, t)$, associated with regression coefficients R_{ij} and U_{ij} (equation 5; Fig. 8). A explains most of the variability of ^{14}CO. At both locations ^{14}CO maximizes in spring, and the abundance of ^{14}CO decreases with increasing SMP. B amounts to a correction of the order of about ± 1 molecule cm^{-3}. Particularly at Arrival Heights, it expresses that ^{14}CO is systematically smaller when $\Delta s < 0$, i.e. the SMP is in its decreasing phase, and vice versa when the SMP is increasing. This hysteresis effect (or lag of the ^{14}CO signal versus the solar forcing) is also present at Baring Head but with a smaller amplitude and a different annual cycle.

The regression fits capture much of the variability of measured ^{14}CO (Fig. 9). Extrapolated to measurements taken during the later period (2010-2021), $\langle^{14}CO\rangle$ systematically overestimates the actual measurements of ^{14}CO at Baring Head. This effect is not evident at Arrival Heights. At Baring Head, this drift indicates a year-round increase in OH noted above, whereas at Arrival Heights, the seasonality of this effect means that Fig. 9 is not suitable for identifying the trend.

Variants of the approach laid out here (we have tested replacing ^{14}CO with its logarithm and with its inverse, and assuming equal weights in the regression) yield essentially the same result for $\langle^{14}CO\rangle$ because it is well constrained by hundreds of observations at both locations. The trend analysis is performed on the normalized measurements $^{14}CO_{norm} = {}^{14}CO/\langle^{14}CO\rangle$ (equation 1; Fig. 2).

When applying this regression analysis to the gridded model results, a simpler ansatz is pursued whereby individually for the 12 months of the year we form

$$\left\langle {}^{14}\mathrm{CO}\right\rangle_m = \sum_{i=0}^{2} P_{im} s(t_m)^i + R_{1,m}\Delta s(t_m). \quad (7)$$

For a given month m of the year, this amounts to fitting by least squares a parabola in s and a term linear in Δs to the monthly-mean ^{14}CO values simulated by the model for this month throughout the data for the period 1989-2009 (21 years). Equation (7) avoids the harmonic expansion in time t (which is unnecessary for the model data, which come as monthly means at regular monthly intervals) and expresses the model-derived $\langle^{14}CO\rangle$ as a function of s, Δs, and month m, thus producing 48 regression coefficients (4 for each month of the year).

Uncertainty calculation

The trend uncertainties in our calculations are made up of two components. One is the statistical uncertainty associated with variability in the climate system. We denote this component as ω. It is quantified as the standard error of the regression coefficients returned by our trend calculation. The other is the instrumental measurement uncertainty (ϵ_k in section "Normalization for seasonal and solar influences"). We assume that these two errors are independent of each other and that for all measurements the measurement error is normally distributed. To combine these two sources of uncertainty into a single uncertainty estimate, we conduct a Monte-Carlo simulation: We produce 10,000 variant realizations of the measurement timeseries with normally distributed random perturbations added to the measurements. For every measurement, the width of this distribution of random additions equals the standard measurement uncertainty. On these 10,000 variant timeseries we then conduct piecewise linear regression analyses and obtain trend estimates t_i and their statistical uncertainties ω_i, where the index i enumerates the randomly perturbed realizations. The best-estimate trend T is then given as $T = \overline{t_i}$; it is practically identical to the central-estimate trend. The combined uncertainty ϵ is

$$\epsilon = \sqrt{\overline{\omega_i^2} + \mathrm{std}^2(t_i)} \quad (8)$$

i.e. ϵ is given as the square root of the sum of the average squared statistical uncertainty $\overline{\omega_i^2}$ (where the ω_i turn out to be similar for all realizations) and the squared standard deviation (std) of the trends t_i associated with the random perturbations, $\mathrm{std}^2(t_i)$. In all cases, the trend errors are increased by less than 50% if the measurement uncertainty is taken into account versus if only the statistical uncertainty is considered. In Fig. 2(b,d), the stated standard (i.e. 68% confidence) trend error estimates reflect the combined measurement and statistical uncertainties calculated using equation (8).

Data availability

The data generated in this study have been deposited in the figshare database under accession code https://figshare.com/s/49f21bb8467336df0948[62].

Code availability

The codes required to reproduce the analysis and plots of this work have been deposited at https://figshare.com/s/49f21bb8467336df0948[62].

References

1. Levy, H. Normal atmosphere: Large radical and formaldehyde concentrations predicted. *Science* **173**, 141–143 (1971).
2. Thompson, A. M. The oxidizing capacity of the Earth's atmosphere: Probable past and future changes. *Science* **256**, 1157–1165 (1992).

3. Lelieveld, J., Dentener, F. J., Peters, W. & Krol, M. C. On the role of hydroxyl radicals in the self-cleansing capacity of the troposphere. *Atmos. Chem. Phys.* **4**, 2337–2344 (2004).
4. Skeie, R., Hodnebrog, O. & Myhre, G. Trends in atmospheric methane concentrations since 1990 were driven and modified by anthropogenic emissions. *Commun. Earth Environ.* **4**, 317 (2023).
5. Hofzumahaus, A., Dorn, H.-P. & Platt, U. Tropospheric OH Radical Measurement Techniques: Recent Developments. In Restelli, G. & Angeletti, G. (eds.) *Physico-Chemical Behaviour of Atmospheric Pollutants: Air Pollution Research Reports*, 103–108 (Springer Netherlands, Dordrecht, 1990).
6. Heard, D. E. & Pilling, M. J. Measurement of OH and HO_2 in the troposphere. *Chem. Rev.* **103**, 5163–5198 (2003).
7. Bousquet, P., Hauglustaine, D. A., Peylin, P., Carouge, C. & Ciais, P. Two decades of OH variability as inferred by an inversion of atmospheric transport and chemistry of methyl chloroform. *Atmos. Chem. Phys.* **5**, 2635–2656 (2005).
8. Liang, Q. et al. Deriving global OH abundance and atmospheric lifetimes for long-lived gases: A search for CH_3CCl_3 alternatives. *J. Geophys. Res.: Atmos.* **122**, 11,914–11,933 (2017).
9. Krol, M. & Lelieveld, J. Can the variability in tropospheric OH be deduced from measurements of 1,1,1-trichloroethane (methyl chloroform)? *J. Geophys. Res.: Atmos.* **108**, https://agupubs.onlinelibrary.wiley.com/doi/abs/10.1029/2002JD002423 (2003).
10. Patra, P. K. et al. Methyl chloroform continues to constrain the hydroxyl (OH) variability in the troposphere. *J. Geophys. Res.: Atmos.* **126**, e2020JD033862 (2021).
11. Naus, S. et al. Constraints and biases in a tropospheric two-box model of OH. *Atmos. Chem. Phys.* **19**, 407–424 (2019).
12. Nicely, J. M. et al. A machine learning examination of hydroxyl radical differences among model simulations for CCMI-1. *Atmos. Chem. Phys.* **20**, 1341–1361 (2020).
13. Rigby, M. et al. Role of atmospheric oxidation in recent methane growth. *Proc. Natl Acad. Sci.* **114**, 5373–5377 (2017).
14. Turner, A. J., Frankenberg, C., Wennberg, P. O. & Jacob, D. J. Ambiguity in the causes for decadal trends in atmospheric methane and hydroxyl. *Proc. Natl Acad. Sci.* **114**, 5367–5372 (2017).
15. Brenninkmeijer, C. A. M., Gromov, S. S. & Jöckel, P. Cosmogenic ^{14}CO for assessing the OH-based self-cleaning of the troposphere. *Radiocarbon* **64**, 761–779 (2022).
16. Szopa, S. et al. Short-Lived Climate Forcers. In Masson-Delmotte, V. et al. (eds.) *Climate Change 2021: The Physical Science Basis. Contribution of Working Group I to the Sixth Assessment Report of the Intergovernmental Panel on Climate Change*, 817-922 (Cambridge University Press, Cambridge, United Kingdom and New York, NY, USA, 2021).
17. Stevenson, D. S. et al. Multimodel ensemble simulations of present-day and near-future tropospheric ozone. *J. Geophys. Res.: Atmos.* **111**, D08301 (2006).
18. Stevenson, D. S. et al. Trends in global tropospheric hydroxyl radical and methane lifetime since 1850 from AerChemMIP. *Atmos. Chem. Phys.* **20**, 12,905–12,920 (2020).
19. Naik, V. et al. Preindustrial to present-day changes in tropospheric hydroxyl radical and methane lifetime from the Atmospheric Chemistry and Climate Model Intercomparison Project (ACCMIP). *Atmos. Chem. Phys.* **13**, 5277–5298 (2013).
20. Voulgarakis, A. et al. Analysis of present day and future OH and methane lifetime in the ACCMIP simulations. *Atmos. Chem. Phys.* **13**, 2563–2587 (2013).
21. Murray, L. T., Fiore, A. M., Shindell, D. T., Naik, V. & Horowitz, L. W. Large uncertainties in global hydroxyl projections tied to fate of reactive nitrogen and carbon. *Proc. Natl Acad. Sci.* **118**, e2115204118 (2021).
22. Chua, G., Naik, V. & Horowitz, L. W. Exploring the drivers of tropospheric hydroxyl radical trends in the Geophysical Fluid Dynamics Laboratory AM4.1 atmospheric chemistry–climate model. *Atmos. Chem. Phys.* **23**, 4955–4975 (2023).
23. Gaubert, B. et al. Chemical feedback from decreasing carbon monoxide emissions. *Geophys. Res. Lett.* **44**, 9985–9995 (2017).
24. Naus, S., Montzka, S. A., Patra, P. K. & Krol, M. C. A three-dimensional-model inversion of methyl chloroform to constrain the atmospheric oxidative capacity. *Atmos. Chem. Phys.* **21**, 4809–4824 (2021).
25. Brenninkmeijer, C. et al. Interhemispheric asymmetry in OH abundance inferred from measurements of atmospheric ^{14}CO. *Nature* **356**, 50–52 (1992).
26. Manning, M., Lowe, D., Moss, R., Bodeker, G. & Allen, W. Short-term variations in the oxidizing power of the atmosphere. *Nature* **436**, 1001–1004 (2005).
27. Krol, M. C. et al. What can ^{14}CO measurements tell us about OH? *Atmos. Chem. Phys.* **8**, 5033–5044 (2008).
28. MacKay, C., Pandow, M. & Wolfgang, R. On the chemistry of natural radiocarbon. *J. Geophys. Res. (1896-1977)* **68**, 3929–3931 (1963).
29. Volz, A., Ehhalt, D. H. & Derwent, R. G. Seasonal and latitudinal variation of ^{14}CO and the tropospheric concentration of OH radicals. *J. Geophys. Res.* **86**, 5163–5171 (1981).
30. Heinrich, W. Cosmic rays and their interactions with the geomagnetic field and shielding material. *Radiat. Phys. Chem.* **43**, 19–34 (1994).
31. Masarik, J. & Beer, J. Simulation of particle fluxes and cosmogenic nuclide production in the Earth's atmosphere. *J. Geophys. Res.: Atmos.* **104**, 12,099–12,111 (1999).
32. Poluianov, S. V., Kovaltsov, G. A., Mishev, A. L. & Usoskin, I. G. Production of cosmogenic isotopes ^{7}Be, ^{10}Be, ^{14}C, ^{22}Na, and ^{36}Cl in the atmosphere: Altitudinal profiles of yield functions. *J. Geophys. Res.: Atmos.* **121**, 8125–8136 (2016).
33. Usoskin, I. G., Alanko-Huotari, K., Kovaltsov, G. A. & Mursula, K. Heliospheric modulation of cosmic rays: Monthly reconstruction for 1951-2004. *Journal of Geophysical Research: Space Physics* **110**, https://agupubs.onlinelibrary.wiley.com/doi/abs/10.1029/2005JA011250 (2005).
34. Vos, E. E. & Potgieter, M. S. New modeling of galactic proton modulation during the minimum of solar cycle 23/24. *Astrophys. J.* **815**, 119 (2015).
35. Bândă, N. et al. Can we explain the observed methane variability after the Mount Pinatubo eruption? *Atmos. Chem. Phys.* **16**, 195–214 (2016).
36. Duncan, B. N. et al. Indonesian wildfires of 1997: Impact on tropospheric chemistry. *J. Geophys. Res.: Atmos.* **108**, https://agupubs.onlinelibrary.wiley.com/doi/abs/10.1029/2002JD003195 (2003).
37. Zhao, Y. et al. On the role of trend and variability in the hydroxyl radical (OH) in the global methane budget. *Atmos. Chem. Phys.* **20**, 13011–13022 (2020).
38. Turnbull, J. C. et al. Sixty years of radiocarbon dioxide measurements at Wellington, New Zealand: 1954-2014. *Atmos. Chem. Phys.* **17**, 14,771–14,784 (2017).
39. Hua, Q. et al. Atmospheric radiocarbon for the period 1950-2019. *Radiocarbon* **64**, 723 – 745 (2021).
40. Jöckel, P. & Brenninkmeijer, C. A. M. The seasonal cycle of cosmogenic ^{14}CO at the surface level: A solar cycle adjusted, zonal-average climatology based on observations. *J. Geophys. Res.: Atmos.* **107**, ACH 23–1–ACH 23–20 (2002).
41. Lassey, K. R., Lowe, D. C. & Smith, A. M. The atmospheric cycling of radiomethane and the "fossil fraction" of the methane source. *Atmos. Chem. Phys.* **7**, 2141–2149 (2007).
42. Hmiel, B. et al. Preindustrial $^{14}CH_4$ indicates greater anthropogenic fossil CH_4 emissions. *Nature* **578**, 409–412 (2020).
43. Li, Y., Xia, Y., Xie, F. & Yan, Y. Influence of stratosphere-troposphere exchange on long-term trends of surface ozone in CMIP6. *Atmos. Res.* **297**, 107086 (2024).

44. Jöckel, P., Brenninkmeijer, C. A. M., Lawrence, M. G. & Siegmund, P. The detection of solar proton produced ^{14}CO. *Atmos. Chem. Phys.* **3**, 999–1005 (2003).
45. Thompson, R. L. et al. Estimation of the atmospheric hydroxyl radical oxidative capacity using multiple hydrofluorocarbons (HFCs). *Atmos. Chem. Phys.* **24**, 1415–1427 (2024).
46. Canadell, J. et al. *Global Carbon and other Biogeochemical Cycles and Feedbacks*, 673-816 (Cambridge University Press, Cambridge, United Kingdom and New York, NY, USA, 2021). https://doi.org/10.1017/9781009157896.007.
47. Petrenko, V. V. et al. An improved method for atmospheric ^{14}CO measurements. *Atmos. Meas. Tech.* **14**, 2055–2063 (2021).
48. Brenninkmeijer, C. A. M. Measurement of the abundance of ^{14}CO in the atmosphere and the ^{13}C/^{12}C and ^{18}O/^{16}O ratio of atmospheric CO with applications in New Zealand and Antarctica. *J. Geophys. Res.* **98**, 10,595–10,614 (1993).
49. Potgieter, M. Solar modulation of cosmic rays. *Living Rev. Sol. Phys.* **10**, 3 (2013).
50. Caballero-Lopez, R. & Moraal, H. Limitations of the force field equation to describe cosmic ray modulation. *J. Geophys. Res.* **109**, A01101 (2004).
51. Usoskin, I., Gil, A., Kovaltsov, G., Mishev, A. & Mikhailov, V. Heliospheric modulation of cosmic rays during the neutron monitor era: Calibration using PAMELA data for 2006-2010. *J. Geophys. Res. – Space Phys.* **122**, 3875–3887 (2017).
52. Herbst, K. et al. On the importance of the local interstellar spectrum for the solar modulation parameter. *J. Geophys. Res.* **115**, D00I20 (2010).
53. Morgenstern, O. et al. Evaluation of the new UKCA climate-composition model - Part 1: The stratosphere. *Geosci. Model Dev.* **2**, 43–57 (2009).
54. Morgenstern, O. et al. Review of the global models used within phase 1 of the Chemistry-Climate Model Initiative (CCMI). *Geosci. Model Dev.* **10**, 639–671 (2017).
55. Zeng, G. et al. Multi-model simulation of CO and HCHO in the Southern Hemisphere: Comparison with observations and impact of biogenic emissions. *Atmos. Chem. Phys.* **15**, 7217–7245 (2015).
56. Zeng, G. et al. Analysis of a newly homogenised ozonesonde dataset from Lauder, New Zealand. *Atmos. Chem. Phys.* **24**, 6413–6432 (2024).
57. Plummer, D. et al. CCMI-2022: A new set of Chemistry-Climate Model Initiative (CCMI) community simulations to update the assessment of models and support upcoming Ozone Assessment activities. *SPARC Newsl.* **57**, 22–30 (2021).
58. IUPAC. IUPAC Task Group on Atmospheric Chemical Kinetic Data Evaluation - Data Sheet HOx_VOC10 https://iupac-aeris.ipsl.fr/datasheets/pdf/HOx_VOC10.pdf (2005).
59. Riahi, K. et al. The Shared Socioeconomic Pathways and their energy, land use, and greenhouse gas emissions implications: An overview. *Glob. Environ. Change* **42**, 153–168 (2017).
60. Rayner, N. A. et al. Global analyses of sea surface temperature, sea ice, and night marine air temperature since the late nineteenth century. *J. Geophys. Res.: Atmos.* **108**, https://agupubs.onlinelibrary.wiley.com/doi/abs/10.1029/2002JD002670 (2003).
61. Mak, J. E., Brenninkmeijer, C. A. M. & Tamaresis, J. Atmospheric ^{14}CO observations and their use for estimating carbon monoxide removal rates. *J. Geophys. Res.: Atmos.* **99**, 22915–22922 (1994).
62. Morgenstern, O. et al. Supporting data and code for "Radiocarbon monoxide indicates increasing atmospheric oxidizing capacity". Available online at: https://figshare.com/s/49f21bb8467336df0948 (2024).

Acknowledgements

The NIWA and GNS Science authors acknowledge the New Zealand Ministry of Business, Innovation, and Employment (MBIE) which, using the Strategic Science Investment Fund (SSIF) and its predecessor funding structures, financed the maintenance of the ^{14}CO measurements since 1989 and the participation of these authors in the writing of this publication. The authors wish to acknowledge the use of New Zealand eScience Infrastructure (NeSI) high-performance computing facilities, consulting support and/or training services as part of this research. New Zealand's national facilities are provided by NeSI and funded jointly by NeSI's collaborator institutions and through the Ministry of Business, Innovation & Employment's Research Infrastructure programme (https://www.nesi.org.nz). This work was also partly supported by the Academy of Finland (grant 354280). We acknowledge Antarctica New Zealand for their logistical support of the Arrival Heights measurements. We furthermore acknowledge Erika Mackay for support with a graphic.

Author contributions

OM and GZ designed this study. OM developed the analysis, implemented the ^{14}CO formulation in NIWA-UKCA, produced the simulations, and led the writing of this paper. GZ is a lead developer of NIWA-UKCA. IU supplied the SMP timeseries and consulted on the production model. MM and GZ advised on the role of ^{14}CO as a constraint on OH. RM, HS, JT, GB, SN, and TB were involved in the collection of the data and data processing. MM developed the storage correction of^{14}CO and oversaw all aspects of the data quality control. All authors contributed to the writing of the paper.

Competing interests

The authors declare no competing interests.

Additional information

Supplementary information The online version contains supplementary material available at https://doi.org/10.1038/s41467-024-55603-1.

Correspondence and requests for materials should be addressed to Olaf Morgenstern.

Peer review information *Nature Communications* thanks Maarten Krol and the other, anonymous, reviewer(s) for their contribution to the peer review of this work. A peer review file is available.